PNAS PLUS

Biological regulation of atmospheric chemistry en route to planetary oxygenation

Gareth Izon[a,1,2], Aubrey L. Zerkle[a], Kenneth H. Williford[b], James Farquhar[c,d], Simon W. Poulton[e], and Mark W. Claire[a,f]

[a]School of Earth and Environmental Sciences & Centre for Exoplanet Science, University of St. Andrews, St. Andrews KY16 9AL, Scotland; [b]Jet Propulsion Laboratory, California Institute of Technology, Pasadena, CA 91109; [c]Department of Geology, University of Maryland, College Park, MD 20742; [d]Earth System Science Interdisciplinary Center, University of Maryland, College Park, MD 20742; [e]School of Earth and Environment, University of Leeds, Leeds LS2 9JT, United Kingdom; and [f]Blue Marble Space Institute of Science, Seattle, WA 98154

Edited by Mark H. Thiemens, University of California at San Diego, La Jolla, CA, and approved February 3, 2017 (received for review November 16, 2016)

Emerging evidence suggests that atmospheric oxygen may have varied before rising irreversibly ∼2.4 billion years ago, during the Great Oxidation Event (GOE). Significantly, however, pre-GOE atmospheric aberrations toward more reducing conditions—featuring a methane-derived organic-haze—have recently been suggested, yet their occurrence, causes, and significance remain underexplored. To examine the role of haze formation in Earth's history, we targeted an episode of inferred haze development. Our redox-controlled (Fe-speciation) carbon- and sulfur-isotope record reveals sustained systematic stratigraphic covariance, precluding nonatmospheric explanations. Photochemical models corroborate this inference, showing $\Delta^{36}S/\Delta^{33}S$ ratios are sensitive to the presence of haze. Exploiting existing age constraints, we estimate that organic haze developed rapidly, stabilizing within ∼0.3 ± 0.1 million years (Myr), and persisted for upward of ∼1.4 ± 0.4 Myr. Given these temporal constraints, and the elevated atmospheric CO_2 concentrations in the Archean, the sustained methane fluxes necessary for haze formation can only be reconciled with a biological source. Correlative $\delta^{13}C_{Org}$ and total organic carbon measurements support the interpretation that atmospheric haze was a transient response of the biosphere to increased nutrient availability, with methane fluxes controlled by the relative availability of organic carbon and sulfate. Elevated atmospheric methane concentrations during haze episodes would have expedited planetary hydrogen loss, with a single episode of haze development providing up to 2.6–18 × 10^{18} moles of O_2 equivalents to the Earth system. Our findings suggest the Neoarchean likely represented a unique state of the Earth system where haze development played a pivotal role in planetary oxidation, hastening the contingent biological innovations that followed.

sulfur mass-independent fractionation | organic haze | planetary oxidation | hydrogen loss | Neoarchean

Quadruple sulfur isotope fractionation is one of the most robust geochemical tools available to constrain the atmosphere's redox state, owing to intrinsic links between atmospheric photochemistry and oxygen (1–11). Prior to ∼2.4 billion years ago (5, 6), sedimentary S-phases display mass-independent S-isotope fractionation (S-MIF; $\Delta^{33}S$ and $\Delta^{36}S \neq 0$),* which is conspicuously absent in the younger geological record (5–7, 11). The disappearance of S-MIF is widely cited as reflecting a critical change in the Earth's atmospheric state, where oxygen exceeded 0.001% of present atmospheric levels (3) during the so-called Great Oxidation Event (GOE; 4–6, 12). More recently, however, the perception of the GOE *sensu stricto* has been questioned by emerging data derived from 3.0–2.5-billion-year-old sedimentary rocks, interpreted to represent both earlier accumulation(s) of atmospheric oxygen/ozone (13–16) as well as transient descents toward a reduced methane-rich atmospheric state (8, 9, 17, 18).

Interrogation of the temporal S-MIF record reveals additional details—variable magnitude and changes in $\Delta^{36}S/\Delta^{33}S$ slope—that are suggested to reflect subtle atmospheric compositional changes beyond the simple presence or absence of oxygen (6–10, 12, 17, 19–21). Specifically, geochemical records from multiple continents reveal a broad correlation between changes in the S-MIF record and highly ^{13}C-depleted organic carbon—termed C-S anomalies (8)—that have been interpreted to reflect the periodic formation of a hydrocarbon haze reminiscent of that observed on Saturn's moon Titan (8–10). Although these records have been used to paint an intriguing picture of Neoarchean atmospheric dynamics in the prelude to the GOE (8, 9), a critical appraisal of the Neoarchean haze hypothesis awaits (22). We present high-resolution, coupled quadruple sulfur- and carbon-isotope, Fe-speciation, and total organic carbon (TOC) records (Fig. 1) from the youngest of the three C-S anomalies identified in core GKF01, obtained from Griqualand West Basin, South Africa (Fig. 1*A*, Fig. S1, *Geological Setting and Age Model*, Dataset S1, and refs. 9, 15, 23, and 24), resulting in the highest temporal-resolution stratigraphic study yet conducted in the Archean. Critical to testing the haze hypothesis, our geochemical records reveal the timing and structure of a C-S anomaly, which when combined with an updated photochemical model demonstrate a connection between changes in $\Delta^{36}S/\Delta^{33}S$ ratios and atmospheric haze.

Significance

It has been proposed that enhanced methane fluxes to Earth's early atmosphere could have altered atmospheric chemistry, initiating a hydrocarbon-rich haze reminiscent of Saturn's moon Titan. The occurrence, cause, and significance of haze development, however, remain unknown. Here, we test and refine the "haze hypothesis" by combining an ultra-high-resolution sulfur- and carbon-isotope dataset with photochemical simulations to reveal the structure and timing of haze development. These data suggest that haze persisted for ∼1 million years, requiring a sustained biological driver. We propose that enhanced atmospheric CH_4, implied by the presence of haze, could have had a significant impact on the escape of hydrogen from the atmosphere, effectively contributing to the terminal oxidation of Earth's surficial environments ∼2.4 billion years ago.

Author contributions: G.I., A.L.Z., S.W.P., and M.W.C. designed research; G.I., K.H.W., J.F., and M.W.C. performed research; G.I., J.F., and M.W.C. contributed new reagents/analytic tools; G.I., A.L.Z., and M.W.C. analyzed data; G.I. wrote the paper; and A.L.Z., K.H.W., J.F., S.W.P., and M.W.C. contributed to writing the paper.

The authors declare no conflict of interest.

This article is a PNAS Direct Submission.

[1]Present address: Department of Earth, Atmospheric and Planetary Sciences, Massachusetts Institute of Technology, Cambridge, MA 02139.

[2]To whom correspondence should be addressed. Email: garethjizon@googlemail.com.

This article contains supporting information online at www.pnas.org/lookup/suppl/doi:10.1073/pnas.1618798114/-/DCSupplemental.

*Sulfur-isotope ratios are conventionally reported in delta (δ) notation and reflect the permil (‰) deviation of the ratio of the least abundant isotope ($^{33,34,36}S$) to the most abundant isotope (^{32}S), relative to the same ratio in an international reference standard (Vienna Canyon Diablo Troilite, V-CDT). For example, $\delta^{34}S = ((^{34}S/^{32}S)_{sample}/(^{34}S/^{32}S)_{V\text{-}CDT}) - 1$. The majority of processes fractionate S-isotopes mass-dependently, whereby $\delta^{33}S \approx 0.515 * \delta^{34}S$ and $\delta^{36}S \approx 1.91 * \delta^{34}S$. Departure from mass-dependent behavior, or mass-independent fractionation (MIF), is expressed in capital-delta (Δ) notation as either non-zero $\Delta^{33}S$ $[(^{33}S/^{32}S)_{sample}/(^{33}S/^{32}S)_{V\text{-}CDT} - ((^{34}S/^{32}S)_{sample}/(^{34}S/^{32}S)_{V\text{-}CDT})^{0.515}]$ or $\Delta^{36}S$ $[(^{36}S/^{32}S)_{sample}/(^{36}S/^{32}S)_{V\text{-}CDT} - ((^{34}S/^{32}S)_{sample}/(^{34}S/^{32}S)_{V\text{-}CDT})^{1.9}]$.

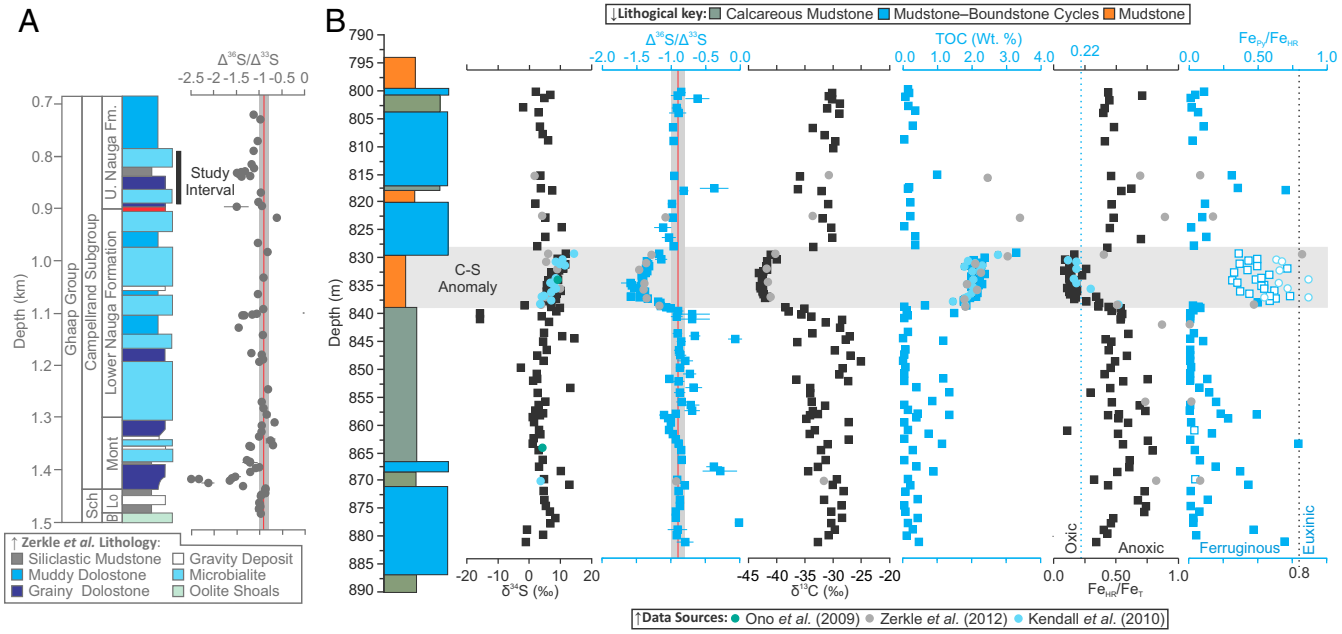

Fig. 1. Preexisting lithological and geochemical data from core GKF01 (9) combined with new high-resolution geochemical data. (*A*) The published low-resolution GKF01 $\Delta^{36}S/\Delta^{33}S$ record (9), the Neoarchean reference array (red line), and its ±0.1 uncertainty envelope (gray vertical band; ref. 8). (*B*) The new $\delta^{34}S$, $\Delta^{36}S/\Delta^{33}S$, $\delta^{13}C$, TOC, and Fe-speciation (Fe_{HR}/Fe_T, Fe_{Py}/Fe_{HR}) data (squares) along with published data (filled circles; refs. 9, 15, and 24). The horizontal gray band signifies the C-S anomaly (discussed in the text). The vertical red line and gray envelope in the $\Delta^{36}S/\Delta^{33}S$ plot represent the Neoarchean reference array and its associated uncertainty (± 0.1; ref. 8). Vertical lines in the Fe-speciation plots distinguish oxic from anoxic ($Fe_{HR}/Fe_T \geq 0.38$) and ferruginous from definitively euxinic ($Fe_{Py}/Fe_{HR} > 0.7$) water column conditions. The open symbols in the Fe_{HR}/Fe_{Py} plot have $Fe_{HR}/Fe_T < 0.22$, signifying oxic sedimentation (9, 15, 67). Assimilating these observations, sedimentation during the examined interval was likely dynamic, with a generally ferruginous background state ($Fe_{HR}/Fe_T > 0.38$; $Fe_{Py}/Fe_{HR} < 0.7$), becoming oxygenated during the C-S anomaly ($Fe_{HR}/Fe_T < 0.22$; ref. 15). The definition of Fe_{HR}, Fe_{Py}, and Fe_T are given as a footnote to the text in *Constraining the Timing and Drivers of Atmospheric Haze Formation*, whereas the derivation of the diagnostic Fe-speciation threshold values are given in *Methodology*, *Sedimentary Fe Speciation*. Analytical uncertainties (1 SD, 1σ) are typically encompassed within each individual data point with the exception of a few $\Delta^{36}S/\Delta^{33}S$ ratios whose uncertainty was computed from larger of the internal or external 1σ uncertainties associated with the raw $\Delta^{33}S$ and $\Delta^{36}S$ data (9). The large-scale lithological log (*A*) follows that presented in Zerkle et al. (9), whereas the new data (*B*) are plotted against the detailed sedimentary logs, which along with core photos are available online (general.uj.ac.za/agouron/index.aspx).

Following this, we speculate on the wider role of episodic haze formation in planetary oxidation.

Results

In core GKF01, the upper Nauga Formation reveals large multiple S-isotope variability, with nonzero $\Delta^{33}S$ and $\Delta^{36}S$ (Figs. 1 and 2, Fig. S2, and Dataset S1), reflecting photochemical production in an atmosphere devoid of significant free oxygen (1–3, 6, 7). The majority of these data form a linear $\Delta^{36}S/\Delta^{33}S$ array (Fig. 2), typifying core GKF01 (9, 18) and the wider Neoarchean as a whole ($\Delta^{36}S \approx -0.9 \times \Delta^{33}S$). Of importance for this study, the $\Delta^{36}S/\Delta^{33}S$ record reveals a coherent stratigraphic structure with a remarkably stable background ($\Delta^{36}S/\Delta^{33}S = -0.9$) punctuated by a spectacular negative excursion between 840.0 and 827.87 m core depth. During the excursion $\Delta^{36}S/\Delta^{33}S$ ratios become increasingly negative (Fig. 1*B*), attaining a steeper slope of ∼−1.5, before relaxing back toward the background $\Delta^{36}S/\Delta^{33}S$ (−0.9; Figs. 1 and 2). Whereas the $\Delta^{36}S/\Delta^{33}S$ data display little variability outside of the identified excursion (Fig. 2), the magnitude of the $\Delta^{33}S$ and $\Delta^{36}S$ is highly variable, carrying positive and negative arithmetic signs, respectively (Fig. S2 and Dataset S1). Consequently, it seems that the dominant sulfur source for pyrite formation over the examined interval was elemental sulfur, inferred to carry a positive $\Delta^{33}S$ (7, 18, 25). Atypically, the $\delta^{34}S$ record displays little variability, with the exception of two relatively more ^{34}S-depleted samples seen at ∼840 m (Fig. 1).

Moving in phase, or perhaps even leading the S-isotope record, $\delta^{13}C_{Org}$ is also observed to descend to extremely low values (less than −37‰; Fig. 1*B*), a relationship that is particularly apparent in Fig. 3*A* where $\Delta^{36}S/\Delta^{33}S$ ratios less than −1 correspond to $\delta^{13}C_{Org}$[†] less than −37‰, and the most ^{13}C-depleted samples relate to the lowest $\Delta^{36}S/\Delta^{33}S$. We observe additional low $\delta^{13}C_{Org}$ values (∼−35‰) below the C-S anomaly that are not associated with changes in $\Delta^{36}S/\Delta^{33}S$ but correspond to small-scale increases in TOC typical of the intercalated mudstones that are below the scale to be illustrated in Fig. 1.

The C-S anomaly is not confined wholly to the mudstone interval, as cursory consideration of Fig. 1 would suggest. The decreases in both geochemical parameters are observed to have occurred by 840-m core depth; however, closer inspection of detailed core logs/photos (Fig. S3, *Geological Setting and Age Model*, and Dataset S1) shows that the lithological change from carbonate to mudstone occurs 0.6–1.0 m above this chemostraigraphic horizon. Similarly, whereas the most depleted $\Delta^{36}S/\Delta^{33}S$ ratios are confined to the basal half of the mudstone, the return to background $\Delta^{36}S/\Delta^{33}S$ is not established until 827.8 m, some 1.5 m above the reestablishment of calcareous sedimentation (Fig. 1, Fig. S3, *Geological Setting and Age Model*, and Dataset S1). These observations require chemostratigraphic controls beyond simple facies or lithological changes.

Discussion

The Causes and Significance of the Sulfur and Carbon Isotope Covariation. The broad correspondence between low $\Delta^{36}S/\Delta^{33}S$ and $\delta^{13}C_{Org}$ has formed the cornerstone of the "haze hypothesis," whereby enhanced methane flux (manifested as low $\delta^{13}C_{Org}$) is hypothesized to have promoted organic-haze formation and altered atmospheric chemistry

[†]Carbon-isotope data are expressed as permil deviations from the Vienna-PeeDee Belemnite (V-PDB) standard: $\delta^{13}C_{Org} = (({}^{13}C/{}^{12}C_{Sample})/({}^{13}C/{}^{12}C_{V\text{-}PDB})) - 1$.

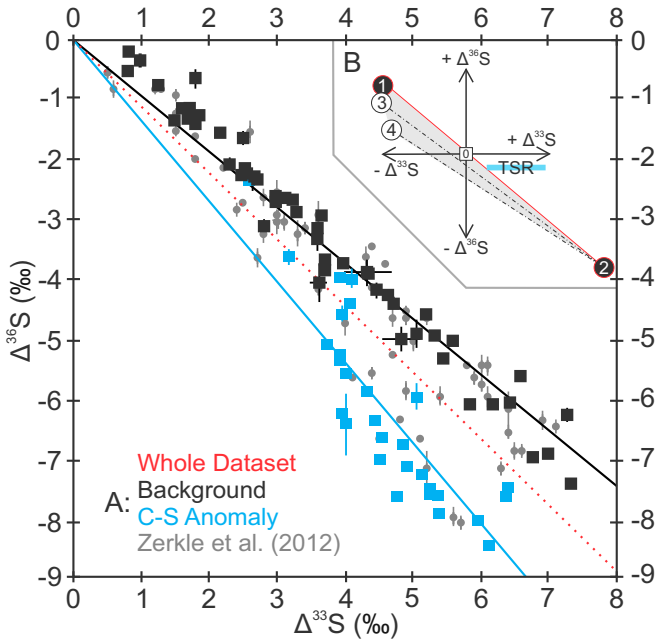

Fig. 2. Quadruple S-isotope data from core GKF01 (*A*) with a schematic mixing scenario (*B*). $\Delta^{36}S$ vs. $\Delta^{33}S$ trends for the new data (black and blue) superimposed on previously published data (gray circles; ref. 9). Regressions are given through the whole dataset (red) as well as through the C-S anomaly (blue) and background (black). Uncertainties are plotted conservatively, using the larger of the internal or external uncertainty (1σ), and are consistently smaller than a single data point. The insert (*B*) schematically illustrates the range of $\Delta^{33}S$ and $\Delta^{36}S$ values that can be expressed in pyrite (shaded gray area) formed via mixing of sulfide derived from MSR (open circles 3–4) with atmospherically derived S-MIF carried by sulfate (filled circle 1) and elemental sulfur (filled circle 2). The horizontal blue bar illustrates the $\Delta^{36}S$-$\Delta^{33}S$ systematics of TSR derived sulfide. Note, biological activity has the potential to exert greater influence on $\Delta^{36}S/\Delta^{33}S$ when pyrite carries a negative $\Delta^{33}S$ (i.e., derived from sulfate) rather than a positive $\Delta^{33}S$ (29) as observed in the C-S anomaly (Fig. 1). Additionally, mixing with TSR-derived sulfide moves the $\Delta^{36}S/\Delta^{33}S$ to less negative values.

(registered as $\Delta^{36}S/\Delta^{33}S$; refs. 8 and 9). The low-resolution records generated in these prior studies, however, have precluded rigorous examination of this hypothesized link, which in turn has obfuscated the wider role of haze formation within the evolution of the ancient Earth system. As a result this early work failed to reveal the stratigraphic structure of a C-S anomaly beyond a few scattered data points. Our geochemical records (Fig. 1, Fig. S2, and Dataset S1) provide a framework from which to examine the origin of the observed C- and S-isotope covariation.

The $\delta^{13}C$ of sedimentary organic matter ($\delta^{13}C_{Org}$) is an integrated product, combining varying contributions from different biological sources. Contemporary and Phanerozoic $\delta^{13}C_{Org}$ records display restricted variability owing to the limited C-isotope fractionation associated with heterotopic respiration. The Neoarchean, by contrast, features a more pronounced range of $\delta^{13}C_{Org}$, indicating more pervasive incorporation of ^{13}C-depleted substrates, particularly methane (26). Accordingly, the low $\delta^{13}C_{Org}$ (<−37‰) seen in the C-S anomaly, and probably the intermediate $\delta^{13}C_{Org}$ (<−35‰) in the basal part of the examined succession (<840 m; Fig. 1), speak to substantial methane incorporation into sedimentary organic matter. In greater detail, this incorporation involves the interplay between localized methane production (methanogenesis), oxidation, and assimilation (methanotrophy; ref. 26). Therefore, the low $\delta^{13}C_{Org}$ data observed in GKF01 (and other Neoarchean sedimentary successions) can be explained in two ways: (*i*) increased methanotrophy assimilating more methane into the sedimentary record independent of the methane flux (26, 27) or (*ii*) enhanced methanogenesis increasing environmental methane availability, with a parallel increase in methanotrophy (8, 9). Sedimentary $\delta^{13}C_{Org}$ values are controlled locally and reflect the carbon utilization strategies of the microbial communities from which the organic matter is sourced. Therefore, the haze hypothesis does not require every inflection in the $\delta^{13}C_{Org}$ record to correspond to altered atmospheric chemistry. In fact, one prediction of the haze hypothesis is that there should be instances where $\Delta^{36}S/\Delta^{33}S$ and $\delta^{13}C_{Org}$ are decoupled (8), such as below 840 m in core GKF01 (Fig. 1).

An Alternate, Nonatmospheric, Control on $\Delta^{36}S/\Delta^{33}S$? The haze hypothesis is reliant on the $\Delta^{36}S/\Delta^{33}S$ parameter faithfully recording what is inferred to be regional to global-scale atmospheric chemistry. The high-resolution dataset we present here (Fig. 1) provides the perfect opportunity to test alternative hypotheses, whereby nonatmospheric, sediment-hosted processes could have produced the observed changes in the $\Delta^{36}S/\Delta^{33}S$ record.

Biological metabolic processes are known to impart small mass-dependent effects during inter- and intracellular (un)mixing processes (19, 28). Biologically mediated mass conservation effects are known to preferentially affect $\Delta^{36}S$, resulting in distinctive $\Delta^{36}S/\Delta^{33}S$ slopes (~−7; ref. 28), potentially overprinting the atmospheric $\Delta^{36}S/\Delta^{33}S$ signal. The extent of such a biological overprint is quasi-predictably governed by initial source of pyrite sulfur, producing a scalene mixing field in $\Delta^{36}S$-$\Delta^{33}S$ quadruple-isotope space (Fig. 2*B* and ref. 29). Because microbial sulfate reduction (MSR) imparts the largest biological S-isotope fractionations, this biological effect is most pronounced when the pyrite sulfur is dominated by a sulfate precursor (negative $\Delta^{33}S$) and becomes progressively more muted when elemental sulfur (positive $\Delta^{33}S$) dominates the pyrite-sulfur pool (29). Examination of Fig. 2, Fig. S2, and Dataset S1 reveals the pyrite throughout the studied interval carries a pronounced and exclusively positive $\Delta^{33}S$, in turn implying an elemental sulfur source, which is expected to be less susceptible to modification by MSR (Fig. 2). In addition to altering $\Delta^{33}S$ and $\Delta^{36}S$, microbial processes are also generally associated with pronounced changes in $\delta^{34}S$ (60–70‰; ref. 30). However, as described above, the $\delta^{34}S$ record in the succession we examined is remarkably stable (Figs. 1 and 3*C*), offering little support for a biologically mediated model (19).

Thermochemical sulfate reduction (TSR) can also impart a distinctive S-MIF signature (Fig. 2*B*); however, this process also cannot explain our S-isotope observations. First, we see no evidence for selective hydrothermal activity associated with TSR in strata between 840.0 and 827.87 m. Decisively, TSR has been shown experimentally to impart large $\Delta^{33}S$ enrichments without significant changes in $\Delta^{36}S$ (31). Addition of TSR-derived sulfur, therefore, would serve to increase $\Delta^{36}S/\Delta^{33}S$ ratios above the Neoarchean reference array, which is contrary to what we observe (Fig. 2).

A final possibility invokes an additional, and isotopically distinct, S-MIF production pathway capable of producing an additional sulfur pool with a distinct and different $\Delta^{36}S/\Delta^{33}S$ (<−1.5), which could selectively contribute to pyrite genesis under variable conditions (32). The observed change in $\Delta^{36}S/\Delta^{33}S$ could, therefore, reflect electron donor availability, highlighting a potential localized control on the degree of pyritization, whereby high TOC permitted selective access to a recalcitrant sulfur pool. Following this scenario, the increased TOC observed in the C-S anomaly (Fig. 1), could potentially provide a sediment-hosted explanation for the observed coupled C- and S-isotope covariation. This explanation would require a ubiquitous association between low $\Delta^{36}S/\Delta^{33}S$, $\delta^{13}C_{Org}$, and high TOC, which is not observed in our data or in previous datasets (Figs. 1–3 and refs. 8, 9, and 22). For example, closer examination of Fig. 3*B* shows there are samples that are enriched in TOC (~1 wt %) yet display typical $\Delta^{36}S/\Delta^{33}S$ ratios

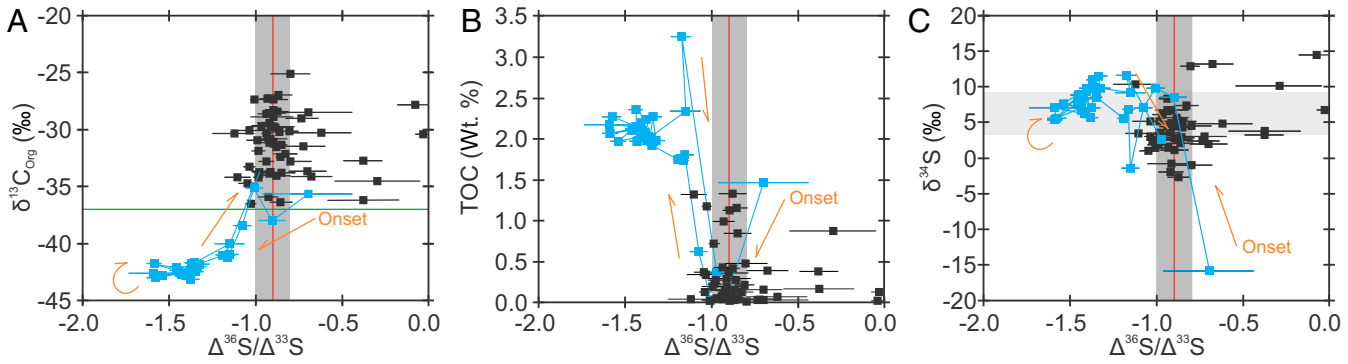

Fig. 3. Carbon isotope ($\delta^{13}C$) (*A*), TOC (*B*), and $\delta^{34}S$ (*C*) vs. $\Delta^{36}S/\Delta^{33}S$ data from 800- to 900-m core depth in core GKF01. In each plot the data have been color-coded, differentiating the background (black) from the C-S anomaly (blue), with orange arrows illustrating its temporal evolution. Vertical red lines in each plot give the average Neoarchean $\Delta^{36}S/\Delta^{33}S$ with a ±0.1 uncertainty envelope (vertical gray bar; ref. 8). The horizontal green line in *A* marks $\delta^{13}C = -37‰$, a threshold commonly used to identify methanotrophy (8, 9, 26). The horizontal gray bar in *C* represents the range of seawater $\delta^{34}S$ estimates derived from carbonate associated sulfate (55). Typically analytical uncertainty is encompassed within the data points, with the exception of a few $\Delta^{36}S/\Delta^{33}S$ ratios as in Fig. 2.

(−0.9). Similar trends are also obvious in published records, with typical $\Delta^{36}S/\Delta^{33}S$ ratios being frequently observed in tandem with high TOC abundances (5% wt %; ref. 9). Also, if sedimentary $\Delta^{36}S/\Delta^{33}S$ ratios were truly independent of time-dependent changes in atmospheric chemistry, the necessary refractory sulfur pool should be ever-present (independent of lithology) and should be observed in other portions of the geological record. For instance, a secondary sedimentary sulfur pool might be expected to be intermittently incorporated into pyrite under a particular range of depositional conditions, producing highly variable $\Delta^{36}S/\Delta^{33}S$ values. This is not the case here (Fig. 1) and is also at odds with the wider Archean $\Delta^{36}S/\Delta^{33}S$ record (19). Moreover, secondary ion mass spectrometry (SIMS) analyses reveal that $\Delta^{36}S/\Delta^{33}S$ trends are conserved at the grain scale between different populations of pyrite within the GKF01 core as a whole (18). Therefore, any model driven by electron donor availability, reliant on a "ghost sulfur pool," cannot be responsible for the observed change in $\Delta^{36}S/\Delta^{33}S$ revealed in the C-S anomaly (Fig. 1). Taken together, sediment-hosted processes, such as biological modification, thermochemical alteration, and differential pyrite genesis, fail to satisfactorily explain the systematic changes in $\Delta^{36}S/\Delta^{33}S$ starting at 840 m, leaving an atmospheric origin as the most parsimonious explanation of these data.

Photochemical Modeling of $\Delta^{36}S/\Delta^{33}S$. Assimilating the arguments presented above, the two isotopic systems (C and S) that form the crux of the haze hypothesis are sensitive to perturbations on different spatial, and potentially temporal, scales. In principle, low $\delta^{13}C_{Org}$, and hence methane production/consumption, should be ubiquitous in the Archean, responding to local-scale changes in organic matter quality and quantity (8, 9, 26). In an atmospheric sense, however, it is unlikely that a short-lived change akin to what we observed in the intercalated subordinate mudstones in the basal part of the succession (>840-m core depth; Fig. 1) would result in a change in atmospheric methane concentrations capable of instigating haze formation. Instead, it would require a sustained regional increase in methane fluxes, caused by changes in nutrient delivery or redistribution in the oceans (discussed below), to plausibly increase atmospheric methane concentrations sufficiently to instigate haze formation. If haze development was substantial enough to enshroud the planet, it is also possible that $\Delta^{36}S/\Delta^{33}S$ could be decoupled from $\delta^{13}C_{Org}$, if the site of methane production/consumption was occurring elsewhere.

To examine the direct link between $\Delta^{36}S/\Delta^{33}S$ values and atmospheric chemistry, we updated and validated an Archean 1D photochemical model (7) to predict $\Delta^{33}S$, $\Delta^{36}S$, and trace $\Delta^{36}S/\Delta^{33}S$ ratios through an atmospheric reaction network (Fig. S4 and *Methodology*, *Photochemical Modeling*). The most significant changes from the initial predictions of Claire et al. (7) arise from the inclusion of new data allowing $\Delta^{36}S$ predictions, and the use of newly measured SO_2 photodissociation cross-sections (33). As noted previously (7, 34), the earlier SO_2 cross-sections (35) produced results at odds to the commonly accepted interpretation of the geologic record: predicting positive $\Delta^{33}S$ in sulfate and negative $\Delta^{33}S$ in elemental sulfur. Incorporating the revised cross-sections (33) resolves this data–model mismatch and now predicts exit channels with the arithmetic sign commonly seen in the rock record (Figs. 4 and 5). However, it is important to note our model still fails to reproduce both the magnitude of the S-MIF and the $\Delta^{36}S/\Delta^{33}S$ ratio archived in the geological record (Figs. 1, 4, and 5, Fig. S2, *Methodology*, *Photochemical Modeling*, and Dataset S1). A detailed exploration of this discrepancy exceeds the scope of this study, but likely reflects uncertainties concerning the primary S-MIF generating mechanism(s) included within the model and/or the composition of the Archean background state (*Methodology*, *Photochemical Modeling* and ref. 7). Both of these potential sources of uncertainty are the focus of ongoing research and remain fundamental to successful inverse reconstruction of the chemical composition of the Archean atmosphere.

Fig. 4*A* provides insight into the transmittance of $\Delta^{36}S/\Delta^{33}S$ ratios through an atmospheric reaction network. Exploiting the putative Neoarchean atmospheric composition (the "standard model") envisaged by Claire et al. (7), sulfur species leave the atmosphere unequally divided between three exit channels. The model predicts that aerosol exit channels (SO_4 and S_8) feature fairly homogeneous $\Delta^{36}S/\Delta^{33}S$ signatures irrespective of the height of their tropospheric genesis. By contrast, the predicted $\Delta^{36}S/\Delta^{33}S$ ratios communicated to SO_2 vary substantially through the troposphere. Sulfur dioxide (SO_2) exits the atmosphere primarily dissolved in rainwater, so homogenization likely precludes the expression of the modeled $\Delta^{36}S/\Delta^{33}S$ variability (Figs. 4 and 5). Aerosol species, by contrast, should serve as more instantaneous vectors carrying the entire range of $\Delta^{36}S/\Delta^{33}S$ to the Earth's surface, resulting in spatial variability independent of atmospheric chemistry. Consequently, the modeled $\Delta^{36}S/\Delta^{33}S$ stability in aerosols is reassuring, advocating $\Delta^{36}S/\Delta^{33}S$ ratios as a conservative parameter reflective of a given atmospheric state; that, unlike the absolute S-MIF magnitude (32), would be unlikely to display significant widespread spatial variability under a truly global atmospheric state. This fits well with the stable background $\Delta^{36}S/\Delta^{33}S$ (−0.9) that is observed throughout the majority of the

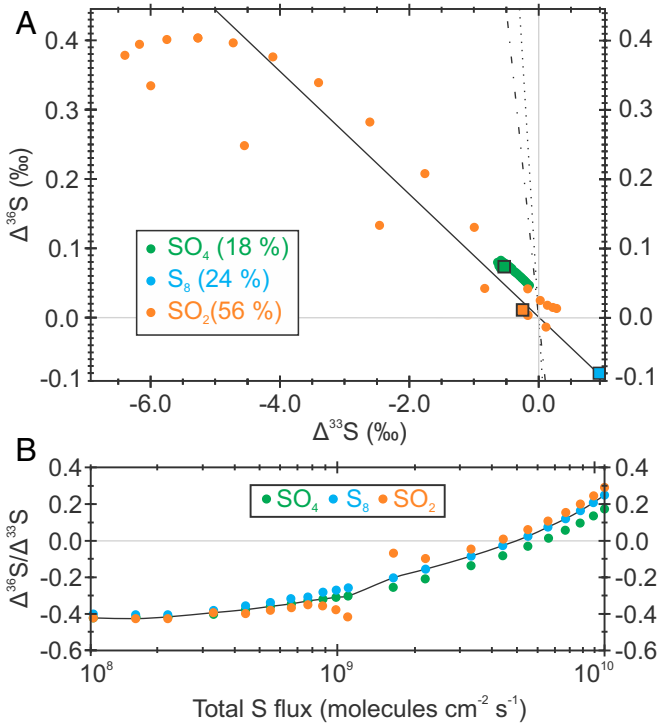

Fig. 4. Photochemical $\Delta^{36}S$ and $\Delta^{33}S$ predictions for the "standard atmosphere" (7) under normal conditions (*A*) and with differential sulfur loading (*B*). Under standard atmospheric conditions, in *A* sulfur leaves the model atmosphere unequally divided between three exit channels (SO_2, 56%; S_8, 24%; and SO_4, 18%). Values of $\Delta^{36}S/\Delta^{33}S$ are displayed for the entire troposphere (filled circles), with the large squares showing the ground-level signal carried by a specific exit channel combining both wet and dry deposition. *B* recreates the experiment illustrated in figures 6 C and D in Claire et al. (7), where the total volcanic sulfur flux to the model atmosphere is varied over two orders of magnitude (10^8–10^{10} molecules^{-2} s^{-1}). The spatial distribution of atmospherically important species within the standard atmospheric framework is displayed in figure 2 of Claire et al. (7), where the following boundary conditions were adopted: volcanic sulfur flux of 3.85×10^9 molecules^{-2} s^{-1} (~1 Tmole y^{-1}) at an H_2S:SO_2 ratio of 1:10 and a volcanic H_2 flux of 1×10^{10} molecules^{-2} s^{-1} (~3 Tmole y^{-1}). Fixed ground-level mixing ratios of 100 ppm and 10 ppb for CH_4 and O_2, respectively. Carbon dioxide concentrations were fixed at 1% at all heights, and N_2 provided a total atmospheric pressure of 1 bar. Full details of the model, validation, and its limitations are appended (*Methodology*, *Photochemical Modeling*).

100 m [11.7 ± 3.3 million years (Myr); *Geological Setting and Age Model*] of examined core (Fig. 1) and the wider Archean record (19).

The utility of $\Delta^{36}S/\Delta^{33}S$ ratios is extended via examination of Fig. 4*B*. Here, we present results from 22 distinct model atmospheres where the total volcanic sulfur flux was varied over two orders of magnitude. This experiment alters the atmospheric redox state, enhancing the relative importance of the S_8 exit channel in the more sulfur-laden atmospheres. Fig. 4*B* shows that within each model atmosphere the $\Delta^{36}S/\Delta^{33}S$ ratios of all exit channels remain homogenous (±0.1), in turn supporting our claim that $\Delta^{36}S/\Delta^{33}S$ reflects the instantaneous state of atmospheric chemistry. The range and systematic decrease in $\Delta^{36}S/\Delta^{33}S$ observed between simulations (+0.2 to −0.4) highlights the sensitivity of $\Delta^{36}S/\Delta^{33}S$ ratios to atmospheric composition, advocating $\Delta^{36}S/\Delta^{33}S$ as a promising atmospheric probe—a conclusion that extends beyond both the chosen experiment (sulfur loading) and our predicted magnitudes.

To examine the ability of an organic haze to modulate $\Delta^{36}S/\Delta^{33}S$, we varied the O_2 and CH_4 fluxes (7, 10) to create two different hazy states (models 1 and 3 in Fig. 5 *B* and *D*) along with an additional clear-skies atmospheric state (model 2 in Fig. 5*C*). Similar to the cases presented previously (Fig. 4*A*), the incorporation of the new cross-sections (33) causes the $\Delta^{33}S$ predictions to deviate from those presented previously (7), qualitatively approximating the geological record. Our simulated hazy atmospheric states produce $\Delta^{36}S/\Delta^{33}S$ slopes (+0.19, Fig. 5*B* and −0.52, Fig. 5*D*) that differ from the clear-skies simulation (−0.04, Fig. 5*C*). The clear-skies simulation in Fig. 5*C* has distinct boundary conditions that are broadly similar to the "standard atmosphere" (Fig. 4*A* and ref. 7) so their similar $\Delta^{36}S/\Delta^{33}S$ provides additional confidence that $\Delta^{36}S/\Delta^{33}S$ slopes are the product of specific atmospheric states and do not vary widely with minor fluctuations in atmospheric state. We stress again that the absolute values of these predictions are preliminary and will likely change with additional model complexity (*Methodology*, *Photochemical Modeling*). Our approach here is not sufficient to make the claim that haze is uniquely responsible for variations in the $\Delta^{36}S/\Delta^{33}S$ slope from −0.9 to −1.5. Rather, our more simple aim is to test the assertion that atmospheric reaction rates, exit channels, and UV transparency vary sufficiently underneath a hazy atmosphere to modulate the $\Delta^{36}S/\Delta^{33}S$ ratios (7–10). The predicted uniformity of $\Delta^{36}S/\Delta^{33}S$ ratios, expressed in all atmospheric exit channels, ultimately facilitates transmission from the atmosphere where they may be preserved in the geological record (8, 9, 18)—a key prediction of the haze hypothesis. Furthermore, the different $\Delta^{36}S/\Delta^{33}S$ ratios produced under different atmospheric hazy regimes provide support to the idea that hazes in different parts of Earth history (e.g., before and after substantial biospheric O_2 fluxes) might yield unique S-MIF signatures (compare Fig. 5*B* and Fig. 5*D*) (8).

A caveat to these inferences hinges on pyrite genesis, the global vs. regional extent of the haze, and the photochemical origin of the pyrite-sulfur precursor. Under a global hazy atmospheric configuration, after mixing into the seawater sulfate reservoir putative hazy-type $\Delta^{36}S/\Delta^{33}S$ ratios (−1.5) would be preserved within pyrite independent of its initial sulfur source (e.g., sulfate or elemental sulfur; Figs. 4 and 5). If regional haze development were possible, then conceivably pyrite could have inherited either a typical Archean $\Delta^{36}S/\Delta^{33}S$ (−0.9) or a steeper hazy-type $\Delta^{36}S/\Delta^{33}S$ (−1.5). Here, elemental sulfur would have carried the atmospheric $\Delta^{36}S/\Delta^{33}S$, and thus the localized instantaneous chemical state directly to pyrite. Contrastingly, pyrite produced from seawater sulfate would be expected to preserve a globally integrated signal, facilitated via oceanic mixing. Therefore, sulfate-sourced pyrite could carry a slope more characteristic of haze beneath a localized clear-skies atmospheric regime. Unfortunately, the current dataset displays exclusively positive $\Delta^{33}S$ (Fig. 2, Fig. S2, and Dataset S1), thus precluding a definitive appraisal of the precursor sulfur (18) in this particular C-S anomaly. Given that our pyrite record is derived from predominantly sulfur aerosols, reflecting instantaneous atmospheric chemistry, the shift in $\Delta^{36}S/\Delta^{33}S$ indicates core GKF01 was deposited beneath a hazy sky, consistent with the observed C- and S-isotope covariation (Figs. 1 and 3*A*).

Constraining the Timing and Drivers of Atmospheric Haze Formation. These geochemical and computational arguments lend credence to the haze hypothesis. Accordingly, we interpret the C-S anomaly as a chemostratigraphic marker of atmospheric haze development. The well-defined structure of the high-resolution C-S anomaly (Fig. 1) allows us to extract time constraints to reveal the tempo and duration of an inferred episode of haze development. Using existing radiometric age constraints (refs. 36–40 and *Geological Setting and Age Model*), and assuming linearity, application of average sedimentation rates suggests that haze persisted for 1.4 ± 0.4 Myr, attaining maximum haze thickness (lowest $\Delta^{36}S/\Delta^{33}S$) over 0.3 ± 0.1 Myr (3 m). Adopting these temporal constraints,

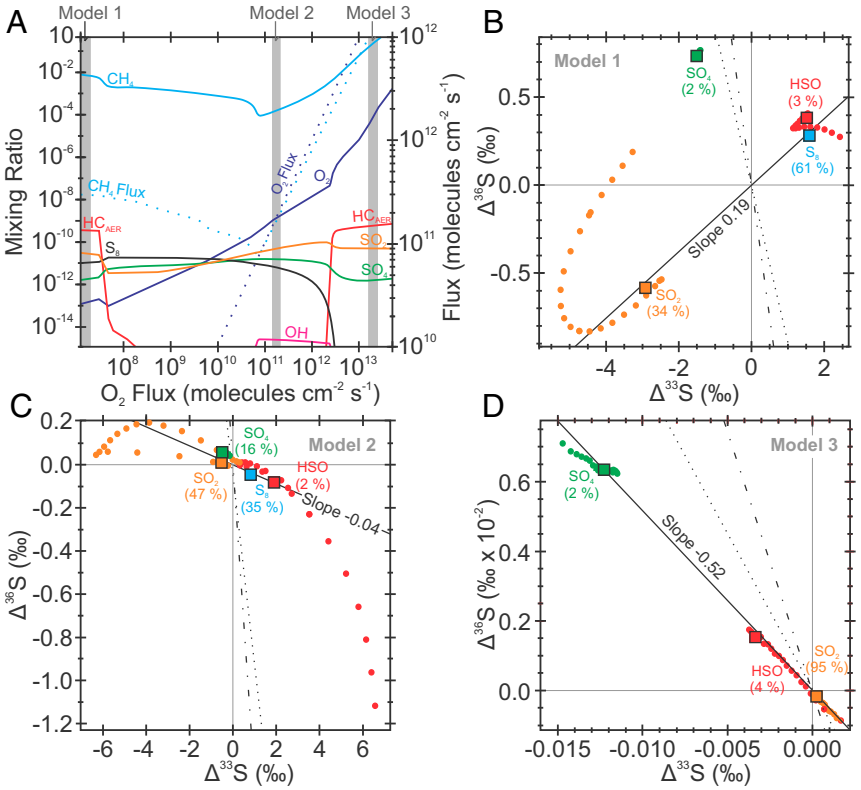

Fig. 5. Simulated $\Delta^{36}S/\Delta^{33}S$ response to varying O_2 and CH_4 fluxes. (*A*) The three distinct atmospheric states (models 1–3, *B–D*) that were chosen to examine the effect of a hydrocarbon haze on atmospheric chemistry (numbered vertical gray bands in *A*). The first model simulates a thick hydrocarbon haze before the advent of oxygenic photosynthesis (*B*), whereas the second and third models represent haze-free (*C*) and hazy (*D*) states after the advent of oxygenic photosynthesis (7, 10). Under each atmospheric regime (*B–D*) the $\Delta^{36}S/\Delta^{33}S$ carried by each atmospheric exit channel, at specific atmospheric height, is plotted as color-coded circles, whereas the atmospherically integrated signal (the ground-level value) of each vector is represented by a color-coded square. The relative importance of each exit channel is given in parentheses. In *A* the mixing ratios of atmospheric species are shown as solid lines (left axis), and fluxes are shown as dashed lines (right axis). In *B–D* the Archean reference array ($\Delta^{36}S/\Delta^{33}S = -0.9$; ref. 8), the steepened slope reflecting the C-S anomaly (Fig. 1) and the best fit to the simulated data are given by the dotted, dot-dashed, and solid lines, respectively. Full details of the model, validation, and its limitations are given in *Methodology*, *Photochemical Modeling*. Zero $\Delta^{36}S$ and $\Delta^{33}S$ data are given as gray lines to illustrate the change in scale between *B–D*.

even acknowledging the potential uncertainties of our approach (*Geological Setting and Age Model*) the development of Neoarchean atmospheric haze is inconsistent with rapid release of methane from a standing methane reservoir (such as methane hydrates) and requires a more sustained methane flux to the atmosphere.

Although contemporary sedimentary methane production is substantial, little escapes to the ocean–atmosphere system owing to efficient consumption by either aerobic methanotrophs or by a consortium of anaerobic methanotrophs and sulfate reducers (AOM) at the sulfate–methane transition zone (41–43). Nevertheless, within the oxygen- and sulfate-starved Neoarchean oceans (44–46) methanogens would have proliferated, whereas methanotrophs and AOM would have been spatially restricted. Correspondingly, enhanced Neoarchean methanogenesis would have likely translated into elevated atmospheric methane fluxes (41–43), supporting large background Archean methane concentrations (7, 10, 20, 21, 41, 47). When the CH_4:CO_2 mixing ratio exceeded a critical threshold of ~0.1 this CH_4 flux would have formed an organic-rich hydrocarbon haze (9, 10, 20, 47), although the regional/global extent of these haze(s) requires further study.

Methanogens feature a complex biochemistry dependent on nickel-based metalloenzymes (48), which they use to produce methane at the expense of simple carbon compounds and molecular hydrogen (49, 50). Although reconstructed marine nickel concentrations suggest that post-2.7-Ga oceans were nickel-limited (49, 50), it is improbable that nickel alone was a stimulus for episodically heightened methane production necessary for haze production. The envisaged Neoarchean oceanic nickel depletion has been attributed to long-term unidirectional mantle cooling, changing the chemical composition of igneous rocks and concomitant marine nickel delivery (49, 50). In contrast, haze formation was geologically rapid and occurred repeatedly in the prelude to the GOE (8, 9), thus requiring a recurrent, yet geologically short-lived, driver. Although it is feasible that episodic volcanism could supply reactive igneous rocks, secular mantle cooling should have ensured their nickel content was progressively lower (49, 50). Perhaps more importantly, it is difficult to envisage a solely volcanic/hydrothermal driver that effectively decouples nickel delivery from other bioessential elements [e.g., P, N, Fe, Mo, etc. (13)].

Alternatively, episodic top-down stimulation of the entire biosphere, via enhanced primary productivity in the surface waters, could provide a more satisfactory trigger for haze development. This inference is supported by relatively high total organic-carbon (TOC) abundances (≥2%) within the C-S anomaly (Fig. 3*B*) compared with the Neoarchean average (1.5 ± 1.3 wt %; ref. 51). Although high TOC abundances could reflect diminished dilution by carbonate, enhanced productivity or preservation, the consistently low primary Fe_{HR}/Fe_T (<0.38) ratios observed during the C-S anomaly (Fig. 1*B*) suggest that

oxic sedimentation persisted[‡] (9, 15), arguing against a preservational control. Contrasting redox inferences gleaned from the S-MIF and the Fe-speciation records further implicate marine productivity with atmospheric haze development. Here, the low Fe_{HR}/Fe_T (<0.38) ratios, in concert with limited enrichments in redox sensitive trace metals [e.g., Mo, Re and U (15)], signal mildly oxic sedimentation against an anoxic atmospheric backdrop (Fig. 1*B*). Given that atmospheric models insinuate O_2 residence times on the order of a few hours (7) and extremely reducing tropospheric conditions, these data can only be reconciled by oxygenic photosynthesis (15) creating locally oxygenated water column conditions and the development of an oxygen oasis (52). The production of oxygen and organic matter in surface environments and their destruction in deeper waters, the sediment–water interface and below, had the potential to spatially decouple oxygen and methane production, thereby offering a mechanism where methane could have escaped water column reoxidation and contributed to the atmospheric methane burden.

Excluding a facies control on the observed TOC increase is more difficult. The deepening experienced during the mudstone deposition probably inhibited carbonate deposition via isolation from the photic zone (23), hence reducing the dilutive effects of the biogenic carbonates during the C-S anomaly. That said, the small-intercalated mudstones in the basal part of the examined section (<840 m) represent the same facies change yet do not display the isotopic covariation that defines the C-S anomaly. This difference we explain as a function of scale: The mudstone containing the C-S anomaly has known lateral facies equivalents in core GKP01 (15, 23, 53), so independent of dilution-type effects, TOC-rich sediments were deposited across a larger area of the Griqualand West basin during the C-S anomaly. Thus, increased TOC deposition could have supplied ample organic carbon to fuel regionally pervasive methanogenesis, potentially enhancing methane fluxes to the atmosphere. Importantly, consistent with the predictions of atmospheric simulations (7), the persistence of large-magnitude S-MIF with changing $\Delta^{36}S/\Delta^{33}S$ (Figs. 1 and 2, Fig. S2, and Dataset S1) demonstrates that the atmosphere remained essentially oxygen-free (1–3, 6, 7, 10) despite evidence for enhanced oxygen production (9, 15). Apparently the global sinks of water column reductants [(e.g., Fe^{2+} (4)], combined with reduced atmospheric gases (e.g., H_2 and CH_4), were still sufficient to prevent atmospheric oxygenation at this time (7, 10).

Deciphering the ultimate stimulus for the inferred biospheric invigoration, and associated ecological shifts, remains difficult, yet given the persistence of large-magnitude S-MIF (Figs. 1 and 2, Fig. S2, and Dataset S1) there is no need to invoke planetary-scale oxidative weathering by free atmospheric O_2 (13, 14). Alternate mechanisms such as episodic chemical weathering driven by changes in climate and/or tectonics could directly, or indirectly (via changes in ocean circulation and upwelling efficiency), have delivered the necessary nutrients to the photic zone over widespread areas. Additionally, the emergence and proliferation of terrestrial life (51) should have also revolutionized weathering efficiency via ground-level oxidative weathering (54), providing another mechanism to flux nutrients (e.g., P and bioessential trace elements), along with sulfate to the ocean, without any significant leak of O_2 to the atmosphere.

Pyrite $\delta^{34}S$ values are lowest at the base of the C-S anomaly (~−15‰) before stabilizing to values close to those reconstructed from contemporaneous carbonate-associated sulfate from the Campbellrand carbonate platform (Figs. 1 and 3*C*, Fig. S2, and ref. 55). Whereas these few ^{34}S-depleted samples could easily reflect changes in sediment-housed microbial sulfur cycling and associated pyrite formation (19, 56), these data can also be reconciled with an initial weathering pulse delivering sulfate, and presumably other nutrients, to the biosphere. Beyond the fortuitous placement of the low $\delta^{34}S$ at the base of the C-S anomaly within an otherwise stable $\delta^{34}S$ record (Figs. 1 and 3*C*), unequivocal discrimination between these two potential explanations of the $\delta^{34}S$ data are challenging on the basis of bulk SF_6 measurements alone. Enigmatically, however, radiogenic $^{187}Os/^{188}Os_i$ ratios have recently been reported from the Mt. McRae shale, which can only be reconciled with crustal ^{187}Os ingrowth via β^- decay of ^{187}Re, followed by remobilization and delivery to the marine reservoir (14). The Mt. McRae succession is perhaps one of the most celebrated Archean sedimentary successions, containing the ~2.5-billion-year-old trace-element enrichments that have been interpreted to represent pre-GOE whiffs of oxygen (13). Interestingly, as noted by Zerkle et al. (9), the upper Mt. McRae shale also features a change in $\Delta^{36}S/\Delta^{33}S$ to lower values (57), which is broadly associated with a change in $\delta^{13}C_{Org}$—exhibiting some interesting parallels with the data presented herein. Unfortunately, the Mt. McRae shale data are of insufficient resolution to make meaningful comparisons with our own, and no Re-Os data exist for the C-S anomaly examined in Fig. 1. Clearly further targeted SF_6 and SIMS analysis, coupled with the application of sensitive radiogenic isotope tracers [e.g., Re-Os (58)], to this and other C-S anomalies (8, 9) has the potential to elucidate the source of the nutrients (weathering vs. oceanic nutrient redistribution) and should be a fruitful avenue of future research.

From an Earth system perspective, low seawater sulfate concentrations were likely an important prerequisite for haze formation, allowing methane to escape AOM in the sediment pile and enter the atmosphere. The Neoarchean oceans as a whole are inferred to have had historically low sulfate concentrations (16, 45), poising the biosphere at a tipping point, allowing the balance between methane production and consumption to shift rapidly following pulses of marine fertilization and attendant sedimentary carbon delivery (8). Consequently, enhanced productivity would be expected to strengthen methane production, creating inflections in the $\delta^{13}C$ isotope record that are only coupled with changes in $\Delta^{36}S/\Delta^{33}S$ when methane fluxes are sufficient to affect atmospheric chemistry. Eventually, however, enhanced terrestrial colonization (51, 54), combined with increasing biological oxygen production (9, 15) and waning availability of residual reductants (e.g., Fe^{2+}), would have changed the marine budgets of electron acceptors [e.g., sulfate (51)], curbing biogenic methane fluxes via enhanced AOM (43) and ultimately changing the atmospheric response to biospheric stimulation (13, 15).

Haze Formation as a Harbinger of Planetary Oxidation? Biogenic methane production has been proposed as an efficient hydrogen shuttle to the exosphere (41). Empirical studies throughout the solar system reveal that multiple processes combine to enable hydrogen escape from the upper atmosphere at its maximum theoretical rate (59), meaning that planetary hydrogen loss can be approximated by the diffusive supply of H-bearing compounds from the stratosphere (e.g., H_2, H_2O, and CH_4). Whereas freeze distillation confines water vapor to the troposphere, methane escapes Earth's cold trap and supplies hydrogen to the stratosphere through photolysis, which can be lost instantaneously to space—irreversibly shedding reducing power and potentially explaining how the Earth's surficial environment became irreversibly oxidized over long timescales (41, 59).

The abrupt change in $\Delta^{36}S/\Delta^{33}S$ correlated to a decrease in sedimentary $\delta^{13}C_{Org}$ seen in the C-S anomaly (Fig. 1*B* and ref. 3)

[‡]Summation of the oxic (Fe_{Carb}, Fe_{Ox} and Fe_{Mag}) and anoxic Fe extractions (Fe_{Py}) defines the highly reactive Fe pool ($Fe_{HR} = Fe_{Carb} + Fe_{Ox} + Fe_{Mag} + Fe_{Py}$), which when normalized to the total Fe pool (Fe_T) and Fe_{Py} permits distinction between oxic (Fe_{HR}/Fe_T = <0.22), ferruginous (Fe_{HR}/Fe_T = >0.38 and Fe_{Py}/Fe_{HR} = <0.7), and euxinic (Fe_{HR}/Fe_T = >0.38 and Fe_{Py}/Fe_{HR} = >0.8) depositional conditions. Details of mineral phases that comprise these operationally defined Fe pools and their empirical derivation are given in *Methodology, Sedimentary Fe Speciation*.

demonstrates a rapid change in atmospheric chemistry, which we have interpreted to represent the development of a hydrocarbon haze formed at elevated methane concentrations. As such, our data and models provide support for the presence of substantial methane in the Archean atmosphere, confirming predictions made in multiple theoretical studies (3, 20, 41–43, 47, 59). Our previous work (8, 9, 17, 18), and the work of others (57), has shown that similar tandem decreases in $\Delta^{36}S/\Delta^{33}S$ and $\delta^{13}C_{Org}$ occur in other Neoarchean strata, suggesting the Neoarchean atmospheric composition was dynamic, and atmospheric haze development was potentially frequent in the overture to the GOE. Experimental data (60, 61) and photochemical models (7, 9, 10, 20, 47) both predict that hydrocarbon hazes form when CO_2:CH_4 mixing ratios exceed ∼0.1. Given the strong dependency of hydrogen escape on atmospheric methane availability (41, 59), conceptually, therefore, intervals of haze development could have served as intervals of heightened hydrogen loss, implicating more reduced atmospheric chemistry as a harbinger of planetary oxidation.

Catling et al. (41) performed three time-resolved calculations where they fixed the partial pressure of CO_2 (pCO_2) (0.0003, 0.003, and 0.01 bar) and calculated the pCH_4 necessary to maintain a surface temperature of 290 K against the evolving luminosity of the Archean sun. Using their figure 1A, pCH_4 was calculated to approximate 950, 170, and 130 ppm when pCO_2 was fixed at 0.0003, 0.003, and 0.01 bar. Simplifying atmospheric pressure to approximate 1 bar equates to background CH_4:CO_2 mixing ratios of 3.16 (950 ppm/300 ppm), 0.06 (170 ppm/3,000 ppm), and 0.01 (130 ppm/10,000 ppm) for each scenario, respectively. Excluding the first scenario because the climatically necessitated CH_4:CO_2 mixing ratio requires the development of a potentially improbably thick organic haze (7, 9, 20, 47) leaves two clear-skies solutions to explore. Assuming organic haze forms when the CH_4:CO_2 mixing ratio exceeds 0.1, haze development in each scenario requires either a 1.67- (0.1/0.06) or 10- (0.1/0.01) fold increase in atmospheric methane concentrations, or a factor of 1.5–10 increase in planetary oxidation rate representing 2.6–18×10^{12} moles O_2 equivalents y^{-1}, assuming the background state was 1–1.5×10^{12} moles O_2 y^{-1}. Consequently, given our estimate of haze duration (1.4 ± 0.4 Myr; *Methodology*, *Geological Setting and Age Model*), a single episode of haze development could equate to a net gain of up to ∼2.6–18×10^{18} moles of O_2 equivalents to the Earth system (41).

It is important to stress that the absolute gain of oxygen equivalents, or the rate of hydrogen loss, depends on both the composition of the atmosphere and on predictions of their resulting climate. Catling et al. (41) used the climate model of Pavlov et al. (62), which has a substantial error in the methane absorption coefficients as rectified by Haqq-Misra et al. (47). When combined with more recent predictions of greenhouse and anti-greenhouse cooling effects (63), Archean pCO_2 in excess of 0.01 is required to warm the planet in lieu of the lower solar luminosity (47). A higher pCO_2 would reduce the background CH_4:CO_2 mixing ratio, requiring a more substantial methane flux to instigate haze formation. Logically, therefore, larger fluxes of methane would promote greater hydrogen escape rates, with concomitant greater oxidative effect, rendering our estimates conservative. A more accurate and precise treatment is dependent on emerging modeling approaches, incorporating more appropriate particle physics and coupled climate modules to calculate accurate radiative transfer through hazy atmospheres (63). However, for now, the most appropriate models reconcile haze development with available geological evidence and suggest that runaway haze development was inhibited by self-shielding (i.e., haze prevents methane photolysis), implicating intricate feedback systems between biological methane production, atmospheric chemistry, and surface-incident UV radiation (63).

Assimilated, core GKF01 reveals a pronounced and stratigraphically systematic excursion toward low $\Delta^{36}S/\Delta^{33}S$ and $\delta^{13}C$ that requires a change in the chemical composition of the atmosphere. This contests the notion of homogenous atmospheric chemistry across vast swaths of Archean time (64) while providing the strongest evidence to date that the Neoarchean was dynamic on million-year time scales. These atmospheric oscillations are best explained via a strong teleconnection between the biosphere and atmospheric chemistry, whereby increased nutrient availability instigated a biogeochemical cascade, prompting organic-haze formation. Episodic haze formation should have hastened hydrogen escape and likely acted as a counterintuitive mechanism of generating significant oxidizing equivalents to the whole Earth system against an oxygen-free atmospheric backdrop.

Methods

The geochemical data presented herein have been generated following established methodologies. Similarly, the photochemical model has been updated, via the inclusion of updated SO_2-photodisasociation cross-sections (33), from that developed in Claire et al. (7). Here, we précis our approach, reserving a complete description for *Methodology*. Briefly, sulfur isotope analysis was performed on purified SF_6, following CRS pyrite distillation, at the University of Maryland (8, 9). Analytical uncertainties are estimated from the long-term reproducibility of Ag_2S fluorinations and estimated to be 0.02, 0.008, and 0.20‰ (1 SD, 1σ) for $\delta^{34}S$, $\Delta^{33}S$, and $\Delta^{36}S$ ratios, respectively. Organic carbon isotope and TOC data were generated at the Jet Propulsion Laboratory (JPL) astrobiogeochemistry laboratory (abcLab) using 10% (vol/vol) HCl decarbonated sample residues. The average reproducibility of $\delta^{13}C_{Org}$ and TOC sample duplicates was found to be ± 0.22‰ and 0.02%, respectively. Iron speciation analyses were conducted at the University of St. Andrews, exploiting an empirically calibrated sequential extraction (65), as detailed in ref. 66, with an extract precision of ∼5%. All raw data are tabulated in Dataset S1.

ACKNOWLEDGMENTS. G.I. thanks S.I., P.I., and C.L.H. for their continued support. The patience and perseverance of two anonymous reviewers is credited for significantly improving this contribution. This study was supported by Natural Environment Research Council (NERC) Fellowship NE/H016805 (to A.L.Z.) and NERC Standard Grant NE/J023485 (to A.L.Z., M.W.C., and S.W.P.). Further financial support was generously provided via a SAGES Postdoctoral & Early Career Researcher Exchange grant and The Geological Society of London's Alan and Charlotte Welch Fund (to G.I.). For his work performed at the Jet Propulsion Laboratory, California Institute of Technology, K.H.W. acknowledges the support of a grant from the National Aeronautics and Space Administration. J.F. acknowledges funding from NASA Exobiology program Grant NNX12AD91G. S.W.P. acknowledges support from a Royal Society Wolfson Research Merit Award. Finally, this project has received funding from the European Research Council (ERC) under the European Union's Horizon 2020 Research and Innovation Programme (Grant Agreement 678812) (to M.W.C.). Final drafting was completed under the auspices of Simons Foundation collaboration on the origins of life at Massachusetts Institute of Technology.

1. Farquhar J, Bao H, Thiemens M (2000) Atmospheric influence of Earth's earliest sulfur cycle. *Science* 289(5480):756–759.
2. Farquhar J, Savarino J, Airieau S, Thiemens MH (2001) Observation of wavelength-sensitive mass-independent sulfur isotope effects during SO_2 photolysis: Implications for the early atmosphere. *J Geophys Res Planets* 106(E12):32829–32839.
3. Pavlov AA, Kasting JF (2002) Mass-independent fractionation of sulfur isotopes in Archean sediments: Strong evidence for an anoxic Archean atmosphere. *Astrobiology* 2(1):27–41.
4. Holland HD (2006) The oxygenation of the atmosphere and oceans. *Philos Trans R Soc Lond B Biol Sci* 361(1470):903–915.
5. Bekker A, et al. (2004) Dating the rise of atmospheric oxygen. *Nature* 427(6970):117–120.
6. Farquhar J, Zerkle AL, Bekker A (2011) Geological constraints on the origin of oxygenic photosynthesis. *Photosynth Res* 107(1):11–36.
7. Claire MW, et al. (2014) Modeling the signature of sulfur mass-independent fractionation produced in the Archean atmosphere. *Geochim Cosmochim Acta* 141:365–380.
8. Izon G, et al. (2015) Multiple oscillations in Neoarchaean atmospheric chemistry. *Earth Planet Sci Lett* 431:264–273.
9. Zerkle AL, Claire MW, Domagal-Goldman SD, Farquhar J, Poulton SW (2012) A bistable organic-rich atmosphere on the Neoarchaean Earth. *Nat Geosci* 5(5):359–363.
10. Kurzweil F, et al. (2013) Atmospheric sulfur rearrangement 2.7 billion years ago: Evidence for oxygenic photosynthesis. *Earth Planet Sci Lett* 366:17–26.
11. Guo Q, et al. (2009) Reconstructing Earth's surface oxidation across the Archean-Proterozoic transition. *Geology* 37(5):399–402.
12. Luo G, et al. (2016) Rapid oxygenation of Earth's atmosphere 2.33 billion years ago. *Sci Adv* 2(5):e1600134.
13. Anbar AD, et al. (2007) A whiff of oxygen before the great oxidation event? *Science* 317(5846):1903–1906.

14. Kendall B, Creaser RA, Reinhard CT, Lyons TW, Anbar AD (2015) Transient episodes of mild environmental oxygenation and oxidative continental weathering during the late Archean. *Sci Adv* 1(10):e1500777.
15. Kendall B, et al. (2010) Pervasive oxygenation along late Archaean ocean margins. *Nat Geosci* 3(9):647–652.
16. Crowe SA, et al. (2013) Atmospheric oxygenation three billion years ago. *Nature* 501(7468):535–538.
17. Williford KH, et al. (2016) Carbon and sulfur isotopic signatures of ancient life and environment at the microbial scale: Neoarchean shales and carbonates. *Geobiology* 14(2):105–128.
18. Farquhar J, et al. (2013) Pathways for Neoarchean pyrite formation constrained by mass-independent sulfur isotopes. *Proc Natl Acad Sci USA* 110(44):17638–17643.
19. Johnston DT (2011) Multiple sulfur isotopes and the evolution of Earth's surface sulfur cycle. *Earth Sci Rev* 106(1–2):161–183.
20. Domagal-Goldman SD, Kasting JF, Johnston DT, Farquhar J (2008) Organic haze, glaciations and multiple sulfur isotopes in the Mid-Archean Era. *Earth Planet Sci Lett* 269(1–2):29–40.
21. Zahnle K, Claire M, Catling D (2006) The loss of mass-independent fractionation in sulfur due to a Palaeoproterozoic collapse of atmospheric methane. *Geobiology* 4(4):271–283.
22. Thomazo C, Nisbet EG, Grassineau NV, Peters M, Strauss H (2013) Multiple sulfur and carbon isotope composition of sediments from the Belingwe Greenstone Belt (Zimbabwe): A biogenic methane regulation on mass independent fractionation of sulfur during the Neoarchean? *Geochim Cosmochim Acta* 121:120–138.
23. Schröder S, Lacassie JP, Beukes NJ (2006) Stratigraphic and geochemical framework of the Agouron drill cores, Transvaal Supergroup (Neoarchean-Paleoproterozoic, South Africa). *S Afr J Geol* 109:23–54.
24. Ono SH, Kaufman AJ, Farquhar J, Sumner DY, Beukes NJ (2009) Lithofacies control on multiple-sulfur isotope records and Neoarchean sulfur cycles. *Precambrian Res* 169:58–67.
25. Ono S, et al. (2003) New insights into Archean sulfur cycle from mass-independent sulfur isotope records from the Hamersley Basin, Australia. *Earth Planet Sci Lett* 213(1–2):15–30.
26. Eigenbrode JL, Freeman KH (2006) Late Archean rise of aerobic microbial ecosystems. *Proc Natl Acad Sci USA* 103(43):15759–15764.
27. Thomazo C, Ader M, Farquhar J, Philippot P (2009) Methanotrophs regulated atmospheric sulfur isotope anomalies during the Mesoarchean (Tumbiana Formation, Western Australia). *Earth Planet Sci Lett* 279(1–2):65–75.
28. Ono S, Wing B, Johnston D, Farquhar J, Rumble D (2006) Mass-dependent fractionation of quadruple stable sulfur isotope system as a new tracer of sulfur biogeochemical cycles. *Geochim Cosmochim* 70(9):2238–2252.
29. Roerdink DL, Mason PRD, Whitehouse MJ, Brouwer FM (2016) Reworking of atmospheric sulfur in a Paleoarchean hydrothermal system at Londozi, Barberton Greenstone Belt, Swaziland. *Precambrian Res* 280:195–204.
30. Canfield DE, Farquhar J, Zerkle AL (2010) High isotope fractionations during sulfate reduction in a low-sulfate euxinic ocean analog. *Geology* 38(5):415–418.
31. Oduro H, et al. (2011) Evidence of magnetic isotope effects during thermochemical sulfate reduction. *Proc Natl Acad Sci USA* 108(43):17635–17638.
32. Halevy I (2013) Production, preservation, and biological processing of mass-independent sulfur isotope fractionation in the Archean surface environment. *Proc Natl Acad Sci USA* 110(44):17644–17649.
33. Endo Y, et al. (2015) Photoabsorption cross-section measurements of ^{32}S, ^{33}S, ^{34}S, and ^{36}S sulfur dioxide from 190 to 220 nm. *J Geophys Res Atmos* 120(6):2546–2557.
34. Lyons JR (2009) Atmospherically-derived mass-independent sulfur isotope signatures, and incorporation into sediments. *Chem Geol* 267(3–4):164–174.
35. Danielache SO, Eskebjerg C, Johnson MS, Ueno Y, Yoshida N (2008) High-precision spectroscopy of ^{32}S, ^{33}S, and ^{34}S sulfur dioxide: Ultraviolet absorption cross sections and isotope effects. *J Geophys Res Atmos* 113(D17):D17314.
36. Knoll AH, Beukes NJ (2009) Introduction: Initial investigations of a Neoarchean shelf margin-basin transition (Transvaal Supergroup, South Africa). *Precambrian Res* 169(1-4):1–14.
37. Altermann W, Nelson DR (1998) Sedimentation rates, basin analysis and regional correlations of three Neoarchaean and Palaeoproterozoic sub-basins of the Kaapvaal craton as inferred from precise U–Pb zircon ages from volcaniclastic sediments. *Sediment Geol* 120(1-4):225–256.
38. Barton ES, Altermann W, Williams IS, Smith CB (1994) U–Pb zircon age for a tuff in the Campbell Group, Griqualand West Sequence, South Africa: Implications for early Proterozoic rock accumulation rates. *Gology* 22:343–346.
39. Gutzmer J, Beukes NJ (1998) High-grade manganese ores in the Kalahari manganese field: Characterization and dating of the ore forming events (Rand Afrikaans University, Johannesburg), p 221.
40. Sumner DY, Bowring SA (1996) U-Pb geochronologic constraints on deposition of the Campbellrand Subgroup, Transvaal Supergroup, South Africa. *Precambrian Res* 79(1-2):25–35.
41. Catling DC, Zahnle KJ, McKay C (2001) Biogenic methane, hydrogen escape, and the irreversible oxidation of early Earth. *Science* 293(5531):839–843.
42. Kharecha P, Kasting J, Siefert J (2005) A coupled atmosphere–ecosystem model of the early Archean Earth. *Geobiology* 3(2):53–76.
43. Beal EJ, Claire MW, House CH (2011) High rates of anaerobic methanotrophy at low sulfate concentrations with implications for past and present methane levels. *Geobiology* 9(2):131–139.
44. Crowe SA, et al. (2014) Sulfate was a trace constituent of Archean seawater. *Science* 346(6210):735–739.
45. Zhelezinskaia I, Kaufman AJ, Farquhar J, Cliff J (2014) Large sulfur isotope fractionations associated with Neoarchean microbial sulfate reduction. *Science* 346(6210):742–744.
46. Guy BM, et al. (2012) A multiple sulfur and organic carbon isotope record from non-conglomeratic sedimentary rocks of the Mesoarchean Witwatersrand Supergroup, South Africa. *Precambrian Res* 216–219:208–231.
47. Haqq-Misra JD, Domagal-Goldman SD, Kasting PJ, Kasting JF (2008) A revised, hazy methane greenhouse for the Archean Earth. *Astrobiology* 8(6):1127–1137.
48. da Silva JJRF, Williams RJP (1991) *The Biological Chemistry of the Elements: The Inorganic Chemistry of Life* (Oxford Univ Press, Oxford).
49. Konhauser KO, et al. (2009) Oceanic nickel depletion and a methanogen famine before the Great Oxidation Event. *Nature* 458(7239):750–753.
50. Konhauser KO, et al. (2015) The Archean nickel famine revisited. *Astrobiology* 15(10): 804–815.
51. Stüeken EE, Catling DC, Buick R (2012) Contributions to late Archaean sulphur cycling by life on land. *Nat Geosci* 5(10):722–725.
52. Olson SL, Kump LR, Kasting JF (2013) Quantifying the areal extent and dissolved oxygen concentrations of Archean oxygen oases. *Chem Geol* 362:35–43.
53. Sumner DY, Beukes NJ (2006) Sequence stratigraphic development of the Neoarchean Transvaal carbonate platform, Kaapvaal Craton, South Africa. *S Afr J Geol* 109:11–22.
54. Lalonde SV, Konhauser KO (2015) Benthic perspective on Earth's oldest evidence for oxygenic photosynthesis. *Proc Natl Acad Sci USA* 112(4):995–1000.
55. Paris G, Adkins JF, Sessions AL, Webb SM, Fischer WW (2014) Neoarchean carbonate-associated sulfate records positive $\Delta^{33}S$ anomalies. *Science* 346(6210):739–741.
56. Bradley AS, et al. (2016) Patterns of sulfur isotope fractionation during microbial sulfate reduction. *Geobiology* 14(1):91–101.
57. Kaufman AJ, et al. (2007) Late Archean biospheric oxygenation and atmospheric evolution. *Science* 317(5846):1900–1903.
58. Cohen AS (2004) The rhenium–osmium isotope system: Applications to geochronological and palaeoenvironmental problems. *J Geol Soc London* 161(4):729–734.
59. Zahnle KJ, Catling DC, Claire MW (2013) The rise of oxygen and the hydrogen hourglass. *Chem Geol* 362:26–34.
60. Trainer MG, et al. (2006) Organic haze on Titan and the early Earth. *Proc Natl Acad Sci USA* 103(48):18035–18042.
61. Hasenkopf CA, et al. (2010) Optical properties of Titan and early Earth haze laboratory analogs in the mid-visible. *Icarus* 207(2):903–913.
62. Pavlov AA, Kasting JF, Brown LL, Rages KA, Freedman R (2000) Greenhouse warming by CH_4 in the atmosphere of early Earth. *J Geophys Res* 105(E5):11981–11990.
63. Arney G, et al. (2016) The pale orange dot: The spectrum and habitability of hazy Archean Earth. *Astrobiology* 16(11):873–899.
64. Thomassot E, O'Neil J, Francis D, Cartigny P, Wing BA (2015) Atmospheric record in the Hadean Eon from multiple sulfur isotope measurements in Nuvvuagittuq Greenstone Belt (Nunavik, Quebec). *Proc Natl Acad Sci USA* 112(3):707–712.
65. Poulton SW, Canfield DE (2005) Development of a sequential extraction procedure for iron: Implications for iron partitioning in continentally derived particulates. *Chem Geol* 214(3–4):209–221.
66. Poulton SW, Fralick PW, Canfield DE (2010) Spatial variability in oceanic redox structure 1.8 billion years ago. *Nat Geosci* 3:486–490.
67. Poulton SW, Canfield DE (2011) Ferruginous conditions: A dominant feature of the ocean through Earth's history. *Elements* 7(2):107–112.
68. Fischer WW, et al. (2009) Isotopic constraints on the Late Archean carbon cycle from the Transvaal Supergroup along the western margin of the Kaapvaal Craton, South Africa. *Precambrian Res* 169(1–4):15–27.
69. Eriksson PG, Altermann W, Hartzer FJ (2006) *The Geology of South Africa*, eds Johnson MR, Anhaeusser CR, Thomas RJ (Geological Society of South Africa, Johannesburg/Council for Geoscience, Pretoria, South Africa), pp 237–260.
70. Canfield DE, Raiswell R, Westrich JT, Reaves CM, Berner RA (1986) The use of chromium reduction in the analysis of reduced inorganic sulfur in sediments and shales. *Chem Geol* 54(1–2):149–155.
71. Clarkson MO, Poulton SW, Guilbaud R, Wood RA (2014) Assessing the utility of Fe/Al and Fe-speciation to record water column redox conditions in carbonate-rich sediments. *Chem Geol* 382:111–122.
72. Raiswell R, Canfield DE (1998) Sources of iron for pyrite formation in marine sediments. *Am J Sci* 298(3):219–245.
73. Anderson TF, Raiswell R (2004) Sources and mechanisms for the enrichment of highly reactive iron in euxinic Black Sea sediments. *Am J Sci* 304(3):203–233.
74. Poulton SW, Raiswell R (2002) The low-temperature geochemical cycle of iron: From continental fluxes to marine sediment deposition. *Am J Sci* 302(9):774–805.
75. Cumming VM, Poulton SW, Rooney AD, Selby D (2013) Anoxia in the terrestrial environment during the late Mesoproterozoic. *Geology* 41(5):583–586.
76. Poulton SW, et al. (2015) A continental-weathering control on orbitally driven redox-nutrient cycling during Cretaceous Oceanic Anoxic Event 2. *Geology* 43(11):963–966.
77. März C, et al. (2008) Redox sensitivity of P cycling during marine black shale formation: Dynamics of sulfidic and anoxic, non-sulfidic bottom waters. *Geochim Cosmochim Acta* 72(15):3703–3717.
78. Pavlov AA, Kasting JF, Eigenbrode JL, Freeman KH (2001) Organic haze in Earth's early atmosphere: Source of low-^{13}C Late Archean kerogens? *Geology* 29(11):1003–1006.
79. Claire MW, et al. (2012) The evolution of the solar flux from 0.1 nm to 160μm: Quantitative estimates for planetary studies. *Astrophys J* 757:1–12.